# TOPOGRAPHY AND DISPLACEMENT OF POLAR GLACIERS FROM MULTI-TEMPORAL SAR INTERFEROGRAMS: POTENTIALS, ERROR ANALYSIS AND VALIDATION

Franz Meyer
Remote Sensing Technology,TU Muenchen, Arcisstrasse 21, D-80333 Munich, Germany - franz.meyer@bv.tum.de

**Commission III, WG III/3**

**KEY WORDS:** SAR, Interferometer, Adjustment, Algorithms, Radar, Modelling, Multitemporal, Environment

## ABSTRACT

This paper describes a new technique to simultaneously estimate topography and motion of polar glaciers from multi-temporal SAR interferograms. The approach is based on a combination of several SAR interferograms in a least-squares adjustment using the Gauss-Markov model. For connecting the multi-temporal data sets, a spatio-temporal model is proposed that describes the properties of the surface and its temporal evolution. Rigorous mathematical modeling of functional and stochastic relations allows for a systematic description of the processing chain. It also is an optimal tool to parameterize the statistics of every individual processing step, and the propagation of errors into the final results. Within the paper theoretical standard deviations of the unknowns are calculated depending on the configuration of the data sets. The influence of gross errors in the observations and the effect of non-modeled error sources on the unknowns are estimated. A validation of the approach based on real data concludes the paper.

## 1 INTRODUCTION

The capability of SAR interferometry (InSAR) in terms of deformation monitoring and topographic mapping has been proven by various case studies during the last decades. In recent years, the focus of investigations has changed towards a detailed analysis of potential error sources, such as temporal and geometrical decorrelation, atmospheric path delay, surface penetration and orbit uncertainties. The analysis of stable targets, so called permanent scatterers, identified from a number of interferograms enables to minimize the effect of temporal and geometrical decorrelation and to remove the influence of the atmospheric path delay. Based on this technique, DEMs with meter accuracy and millimeter terrain motion detection can be derived. However, due to the lack of stable targets, this method can not be applied for the analysis of glaciers and ice sheets, which is a well known application of InSAR. Thus, the evaluation of possible error sources is still a challenging problem in glacier monitoring.

This paper presents an estimation method to determine topography and motion of polar ice masses from SAR interferograms. The approach is focused on a systematic modeling of all processing steps and their particular stochastic properties. The functional and stochastic description of all influences on the interferometric phase signal serves as basis for a detailed accuracy, robustness and error analysis of the estimated results. Special emphasis is put on the investigation of influences from topography and motion, as well as the effects of orbit errors, atmospheric path delays, and the penetration depth of the signal into the surface.

## 2 METHOD

### 2.1 Adjustment model

The aim of all adjustment methods is to map a number of $n$ erroneous observations $b$ on a number of $u < n$ unknown parameters $x$. To make this step possible it is indispensable to formulate functional relations between observations and unknowns. *The functional model* of a least-squares adjustment based on erroneous observations is defined by

$$b + \hat{\varepsilon} = f(\hat{x}_1, \hat{x}_2, \hat{x}_3, ..., \hat{x}_{u-1}, \hat{x}_u) \qquad (1)$$

with $\hat{\varepsilon}$ being the estimated values of residuals and the estimated unknowns $\hat{x}_i$. If accuracy measures for the observations are available, weighting of the observations may be performed. Observations with high accuracy will get high weights and will therefore have strong influence on the estimated parameters and vice versa. The a priori information about the accuracy of the observations is called *stochastic model* and is arranged in the so called covariance matrix $K_{bb}$.

Using the Gauss-Markov theory the optimal solution of a overdetermined equation system as shown in Equation (1) is derived by minimizing the objective function $\delta$:

$$\delta = \hat{\varepsilon}^T P_{bb} \hat{\varepsilon} \quad \rightarrow \quad min \qquad (2)$$

with $P_{bb} = K_{bb}^{-1}$. Solving this minimization problem yields the adjusted unknowns $\hat{x}$ as well as their theoretical accuracies expressed by the $Q_{\hat{x}\hat{x}}$ matrix

$$\hat{x} = \Delta\hat{x} + \overset{\circ}{x} \;=\; \left(A^T P_{bb} A\right)^{-1} A^T P_{bb} b + \overset{\circ}{x} \qquad (3)$$

$$Q_{\hat{x}\hat{x}} \;=\; \left(A^T P_{bb} A\right)^{-1} \qquad (4)$$

with $A$ comprising the functional relations and $\overset{\circ}{x}$ containing approximate values for the unknowns (Mikhail, 1976).

### 2.2 Observations and unknowns

Based on observations derived from SAR data the unknown topography $h$ and motion $v = \frac{\delta r}{\Delta t}$ of polar glaciers are estimated. Within the adjustment, only that component of the surface movement that lies in the line of sight of the sensor can be determined. Thus, $v$ always corresponds to the line of sight component of surface motion.

SAR SLC's of the ERS C-band SAR serve as primary data source. From this data sets $N$ SAR interferograms are formed. Unfortunately, the temporal baseline $\Delta t$ of the interferograms can not be arbitrarily chosen. $\Delta t$ is above all limited by temporal decorrelation. Especially in snow covered polar regions changing wind conditions, temperature variations, and precipitation result in a strong decrease of correlation with time. To warrant interferograms with sufficient quality, only interferograms originating from the ERS tandem mission are considered, which comprise a temporal baseline of only a single day. The ambiguous interferometric phase values are unwrapped based on a minimum spanning tree approach before implementing them into the adjustment. In addition a reference phase screen is subtracted from the interferograms in beforehand using ERS D-PAF precision orbit information.

### 2.3 Functional model

As described above, the functional model comprises the deterministic relations between observations an unknowns. For solving the proposed problem, three different sub-models are necessary. The formulation of the sub-models and their particular characteristics are derived in the following.

**2.3.1 Interferometric model** Although the phase $\phi$ of an interferogram acquired over glaciated terrain is influenced by many parameters, $\phi$ is dominated by influences from surface topography $h$, coherent senor motion $v$ in line-of-sight of the sensor, the difference of the slant-atmospheric delay $\Delta sd$ between the two acquisitions, and the penetration depth $d$ of the RADAR signal into the glacier surface. The unwrapped interferometric phase at position $(i, j)$ of an interferogram can be written as

$$\begin{aligned}\phi^{i,j}_{unw} &= -\frac{4\pi}{\lambda}\left(\frac{B^{i,j}\cos(\theta^{i,j}-\alpha^{i,j})}{r^{i,j}\sin(\theta^{i,j})}h^{i,j} + v^{i,j} + \Delta sd^{i,j}\right) \\ &\quad - \arctan\left(-\frac{2\pi\cdot\sqrt{\epsilon'}\cdot d^{i,j}\cdot B^{i,j}_{\perp}}{r^{i,j}\lambda\tan(\theta^{i,j})}\right) \qquad (5)\end{aligned}$$

The notation used in the equation is in accordance with (Hanssen, 2001). The four different parts of Equation (5) show the mathematical description of the above mentioned influences onto the interferometric phase. The geometric reference phase is already corrected in this representation. According to Equation (5) each interferometric phase observation induces 4 unknown parameters ($h$, $v$, $\Delta sd$, $d$). Thus, the inversion of the model is a highly underdetermined problem. A solution can be found if *i*) additional observations are incorporated on a pixel by pixel basis, or if *ii*) prior information is integrated into the equation system. The second strategy might be employed if one or more parameters of the equation system are known (e.g. external DEM's, or knowledge about surface deformation). Such information is mostly not available in the arctic environment. Thus, a solution has to be found by a combination of a series of interferograms in consideration of additional assumptions about the time evolution of some parameters.

**2.3.2 Temporal model** To guarantee a successful separation of the phase components in Equation (5) functional relations describing the connection between unknowns in different data sets have to be established. Such models are only found for deterministic processes, i.e. signals that do not arise from a stochastic process. In principle, this holds only for the evolution of topography and surface displacement. As topography changes are usually slow, and because of the limited sensitivity of the interferometric phase with respect to topography variations, a time independent description of surface topograpy $h$ has been chosen. Introducing this model reduces the amount of topography-related unknowns from $N \cdot i \cdot j$ unknowns to $i \cdot j$ unknowns. As described in (Fatland and Lingle, 1998) and (Frolich and Doake, 1998) the assumption of constant glacier flow is doubtful especially if ERS tandem interferograms are used. For modeling a time-dependent flow behavior $v(t)$ a mathematical model is employed. We refrain from using physical flow models, because of their high complexity, significant non-linearity, and limited quality. As least-squares adjustments are better suited for solving linear problems, linear models for describing the glacier flow are favored. Considering the usually uneven distribution of the data sets over time a piecewise Lagrange polynom is selected. The maximum polynomial order $\bar{u}$ is equal to $\bar{u} = N - u_v - 1$, where $u_v$ is the number of parameters not related to surface motion. The term $-1$ warrants a redundant equation system. Thus, the surface motion $v(t)$ is modeled by

$$v(t) = \sum_{g=1}^{N-\bar{u}} a_g t^{g-1} \qquad (6)$$

**2.3.3 Spatial model** The unknown parameters are not solved in each pixel but rather in the nodes of a regular spatial grid. This step is allowed if the sampling rate of the digital data sets is higher than necessary for the representation of their information content. The restriction of calculating the desired parameters only in a coarser grid entails several advantages. On one hand, it reduces processing time, on the other hand, it increases redundancy and, by this, the ability of the adjustment to detect gross errors in the observations. The mesh size has to be chosen properly to avoid undersampling. Bilinear planes have been selected for approximating the spatial correlation of topography and motion. The functional relation between an observed phase value in an arbitrary position $\phi^{i,j}$ and an unknown value in a node of the corresponding bilinear raster $\phi^{k,l}$ is given by

$$\begin{aligned}\phi^{i,j} &= \phi^{k,l} + (\phi^{k+1,l} - \phi^{k,l})dr + (\phi^{k,l+1} - \phi^{k,l})dc + \\ &\quad (\phi^{k+1,l+1} - \phi^{k+1,l} - \phi^{k,l+1} + \phi^{k,l})drdc \qquad (7)\end{aligned}$$

where $dr = \phi^i - \phi^k$ and $dc = \phi^j - \phi^l$.

Although using the proposed models allows to reduce the number of unknowns, the equation system is still underdetermined. This is due to the un-modeled atmospheric artifacts and the unknown penetration depth. In (Hanssen, 2001) a stochastic model for approximating the influence of the atmosphere on SAR interferograms is proposed, which is based on the spatial correlation of the atmospheric signal. As the atmosphere in the arctic area can not hold much water vapor and is usually characterized by a stable stratification, atmospheric effects are neglected in this study. The penetration depth of C-band SAR signals into firn and ice was studied in detail in (Hoen, 2001). Maximal penetration depth into dry snow is shown to be up to 30 m. In this paper penetration depth is considered constant in time. Influences by constant penetration depth is considered as part of the topography component.

### 2.4 Stochastic model

Weighting of observations is done by considering the coherency of the observed phase values. The probability density function (PDF) of the interferometric phase for each resolution cell is calculated from the coherency using the theory described in (Bamler and Hartl, 1998) and (Lee et al., 1994). The standard deviations of the observed phase values are derived from the PDF function by

$$\sigma_\phi = \int_{-\phi}^{\phi} (\phi - \phi_0)^2 PDF(\phi) dt \qquad (8)$$

with $\phi_0$ being the expectation value of the interferometric phase. From the standard deviations the weight matrix $P_{bb} = diag\frac{1}{\sigma_{ii}^2}$ is set up. The stochastic model derived in this way implicitly accounts for noise introduced by temporal, thermal and geometric decorrelation as well as errors originating from imperfect interpolation and co-registration procedures.

Additional variance and covariance values are usually introduced by orbit errors and atmospheric effects. These additional error sources are neglected in this study for the following two reasons: (1) Orbit errors have been significantly reduced using control point information. (2) Atmospheric effects showed to be small in polar regions as their cold atmosphere appears to be very stable and can not hold much water vapor. A closer look on atmospheric effects is included in section 3.

## 3 ANALYSIS OF THE APPROACH

### 3.1 Accuracy analysis

The diagonal of $Q_{\hat{x}\hat{x}}$, which contains information about the variances of the adjusted parameters, is used to derive theoretical standard deviations of topography $\sigma_{topo}$ and surface motion $\sigma_{disp}$. For analyzing the accuracy of the approach, simulated data sets have been generated on the basis of existing DEM and velocity maps. The coherency estimates of each interferogram account for the local surface slope. The dependency of $\sigma_{topo}$ and $\sigma_{disp}$ on the number of independent data sets is shown in Figure 1. The improvement, which can be attained if more than two interferograms are combined for estimating the unknown parameters, is clearly visible.

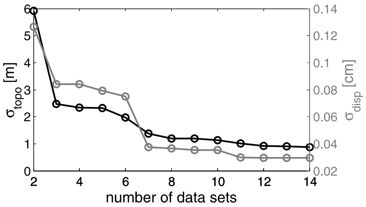

Figure 1: Theoretical standard deviations $\sigma_{topo}$ (black) and $\sigma_{disp}$ (gray) dependent on the number of data sets.

Figure 2 shows how the standard deviations of the estimated topography and displacement parameters depend on the observation geometry, which is mainly a function of the interferometric baseline $B$. The presented results are calculated on the basis of 3 simulated interferograms. In 256 simulation runs, the baselines of the interferograms 1 and 2 are varied from 0 m to 400 m each. The baseline of the third interferogram is fixed at 200 m. In general, the standard deviations of both, topography and motion, show distinct dependency on the baseline ratio of the involved interferograms. Baselines of similar length result in a weak configuration of the adjustment model and finally, in increased values for $\sigma_{topo}$, and $\sigma_{disp}$. In case of identical baselines the adjustment get's singular (this case is indicated by the cross in Figure 2). If the baselines of the 3 interferograms are well distributed, the topographic height may be estimated with an accuracy of $\sigma_{topo} \approx 3$ m and the surface motion with a standard deviation of $\sigma_{disp} \approx 1 - 2$ mm/day. More detailed inspection of Figure 2 shows however, that topography- and displacement-uncertainties are not minimized by the same measurement setup. $\sigma_{topo}$ is decreasing for well distributed long baselines, optimal accuracies of surface motion arise if all baselines are short.

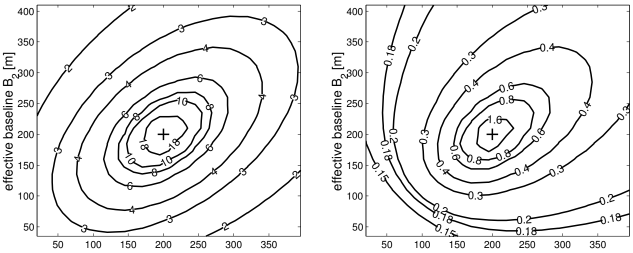

a) b)

Figure 2: *a*) Mean standard deviation of topography (m) and *b*) mean standard deviation of displacement parameters (mm/day) as a function of baseline constellation. The effective baseline length of $B_3$ ist set to 200 m.

### 3.2 Sensitivity regarding model errors

The interferometric model presented in Equation (5) has been simplified by neglecting the influences of atmospheric effects and penetration depth. If these non-modeled influences are significant, model errors are introduced resulting in a systematic falsification of the estimated unknowns.

**3.2.1 Atmospheric effects** Because of the relative character of an interferogram, the theoretical expectation value of atmospheric effects will be zero for an arbitrary pixel. However, the variance of the signal might be significant depending on the respective weather conditions. If enough observations are combined, the empirical expectation value, which is estimated from the data, converges the theoretical value. Thus, for large amount of observations, atmospheric effects will cancel out. The effect of non-modeled atmospheric influences on the estimated unknowns has been calculated for varying observation configurations. Atmospheric phase screens have been simulated based on a method presented in (Hanssen, 2001) considering the effect of the polar atmosphere on the interferometric phase as described in (Gray et al., 1997). Figure 3 shows the effect of the polar atmosphere on the unknown topography $h$ and motion $v$ as a function of the number of multi-temporal data sets. The solid lines in Figure 3 shows the systematic error of the estimated topography (Figure 3*a*)) and motion (Figure 3*b*)). For a low number of data sets, topography may be falsified up to $\Delta h = 10$ m, the estimated motion up to $\Delta v = 0.4$ cm/day. With increasing number of data sets $\Delta h$ and $\Delta v$ converge zero as expected. For investigating whether $\Delta h$ and/or $\Delta v$ differ significantly from zero, a significance test is performed. The dashed lines in Figure 3 represent the upper acceptance limit for the null hypothesis. Values lying above the dashed line are significant, values below insignificant. Figure 3 shows that in arctic regions systematic errors of the adjusted unknowns due to atmospheric effects are insignificant for all tested configurations.

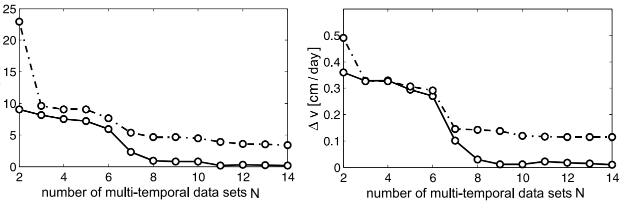

a) b)

Figure 3: Effect of non-modeled atmospheric effects on the estimated unknowns topography (*a*)) and motion (*b*)) for polar regions.

**3.2.2 Penetration depth** The penetration depth $d$ into the glacier surface depends mainly on its physical properties. As presented in (Hoen, 2001), C-band signals penetrate up to 27±5 m into cold firn. The impact $\phi_{pd}$ on the interferometric phase increases with the interferometric baseline. Figure 4 shows the dependence of $\phi_{pd}$ on $d$ and $B$. A time independent $d$ results in a

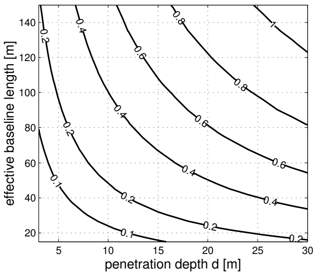

Figure 4: Effect of penetration depth on the interferometric phase [rad].

systematic under-estimation of the glacier topography. The topographic height error is given by

$$\Delta h_{pd} = \frac{\lambda r \sin(\theta)}{4\pi B_{\perp}} \phi_{pd} \tag{9}$$

Considering a typical baseline of B=100 m a height error $\Delta h_{pd}$ of up to 100 m might occure.

**3.2.3 Improperly chosen temporal model** An improperly chosen temporal model may also introduce systematic errors. In common dInSAR approaches the flow of a glacier is usually considered as constant in amplitude and direction for the complete observation period. Errors due to violations of this simplified flow model are analyzed based on simulated data sets. The topography related phase is simulated based on a DEM of a test glacier (Sonklar glacier, Hall-Island, Franz-Josef Land). The motion part of the phase increases linearly with time and is derived from Equation (6). The surface velocity field at time $t = 0$ is simulated based on the known velocity field of the same test glacier. Tests with varying acceleration rates showed that the resulting systematic errors are significant for all test scenarios and for both, topography and motion. Increasing the number of data sets allows to significantly reduce the topography error $\Delta h$, but motion errors appear nearly unchanged.

## 4 VALIDATION

In this section the presented estimation method is validated based on multi-temporal data sets of a test area in the high Russian arctic. Hall Island is one of the largest islands of the Russian archipelago Franz-Josef Land. Approximately situated at 80° 10' N and 58° 05' E, its variety of topographical and glaciological forms as well as drastic changes of its environment attracts the attention of glaciologists. An impression of Hall Island is given in Figure 5. Approximately 90 % of the island is covered by the so called Moscow Ice Dome whose ice masses flow into the sea along several large outlet glaciers. Ice free areas appear mainly in the north of Hall Island and on the two headlands in the south-east (hatched areas in Figure 5). Nearly 50 % of the shoreline is dominated by the calving ice fronts of the large outlet glaciers. Some information about the most important outlet glaciers on Hall Island is included in Table 1. The numbers in the first column of Table 1 correspond to the numbering in Figure 5.

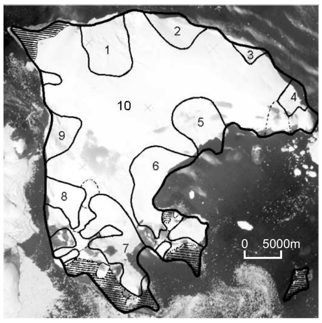

Figure 5: KATE-200 image of Hall Island, Franz-Josef Land superimposed by a coarse information about its coastline and glacier margins taken from (Vinogradov and Psaryova, 1965).

| Number | Name | Area $[km^2]$ | Length $[km]$ |
|---|---|---|---|
| 1 | Sonklar | 54.0 | 9.0 |
| 2 | Nr. 2 | 25.2 | 5.5 |
| 3 | Nr. 3 | 6.0 | 2.6 |
| 4 | Nr. 4 | 13.3 | 4.5 |
| 5 | Nr. 7 | 47.1 | 9.8 |
| 6 | Nr. 8 | 67.0 | 6.1 |
| 7 | Nr. 12 | 56.7 | 8.5 |
| 8 | Nr. 16 | 23.1 | 7.7 |
| 9 | Nr. 17 | 33.6 | 5.8 |
| 10 | Moscow | 504.7 | 30.0 |

Table 1: Information about the largest outlet glacier on Hall Island according to (Vinogradov and Psaryova, 1965).

### 4.1 Data sets

During the tandem- and ice-phase mission of the ERS1/2 satellite system several data sets were acquired over the area of interest. 6 ERS SAR SLC's recorded during the ERS1/2 tandem mission were chosen for further processing. Meteorological data has been included in the selection process to warrant comparable atmospheric conditions for all observations. All images are acquired in 1995 and cover the period from summer until winter of the mentioned year. The properties of the data sets are shown in Table 2. The interferometric processing of the complex SAR images has been accomplished with the *Doris v3.6* software developed at the *Delft Institute for Earth-oriented Space Research* of the Technical University Delft, NL. The Phase and coherency image of a subset of the September interferogram that covers Hall Island, are shown in Figure 6. Areas with large displacement related phase components are marked with white frames. The framed regions correspond to the catchment areas of the outlet glaciers Sonklar, Nr. 7, Nr. 8, Nr. 12 and Nr. 17 (consult Table 1 and Figure 5). In order to utilize the data for usage in the estimation process, some preprocessing steps are necessary. The most important step is the unwrapping of the initially ambiguous interferometric phase values. In addition the data sets are co-registered and phase ramps originating from orbit errors are removed based on control point information.

| Satellit | Datum | Flugricht. | Basislinie ($\|\|$) | Basislinie ($\perp$) |
|---|---|---|---|---|
| ERS1 | 03.09.1995 | desc | -19 m | -50 m |
| ERS2 | 04.09.1995 | | | |
| ERS1 | 08.10.1995 | desc | 57 m | 129 m |
| ERS2 | 09.10.1995 | | | |
| ERS1 | 17.12.1995 | desc | -9 m | -43 m |
| ERS2 | 18.12.1995 | | | |

Table 2: Properties of used SAR data.

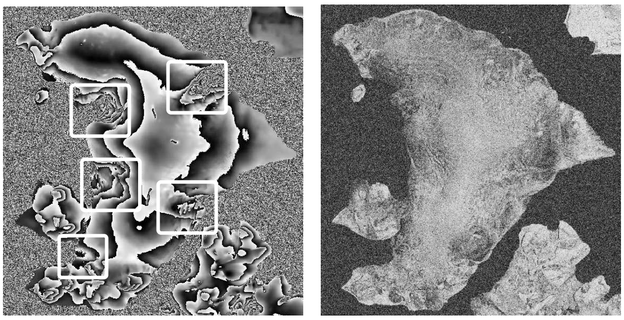
*a*)
*b*)

Figure 6: Phase image (*a*)) and coherency image (*b*)) of the September interferogram of Hall Island. The baseline of the interferogram is $\approx 50\,\mathrm{m}$.

### 4.2 Estimation results

The preprocessed data sets form the vector of observations $b$ in the estimation approach. Within the adjustment the unknown topography and motion parameters are estimated in the nodes of the chosen spatial model (see Section 2.3.3). To reduce the computational load the area of interest is separated into 14×14 tiles, which are evaluated separately and re-merged afterwards. Finally, topography and motion values in all resolution cells $(i, j)$ are interpolated from the estimated unknowns in the bilinear gird based on the mapping function of the spatial model. Thus, an area-wide DSM and velocity field is available after the process.

**4.2.1 Digital surface model of Hall Island** Figure 7 shows the DSM of Hall Island derived from the interferometric phase using the proposed method. The topographic height values shown in Figure 7 are referenced to the WGS84 ellipsoid and vary within 0 m - 500 m. The topography gradient is small in the glaciated terrain. Rough terrain only appears in the mountainous regions in the south-western and eastern parts of the island.

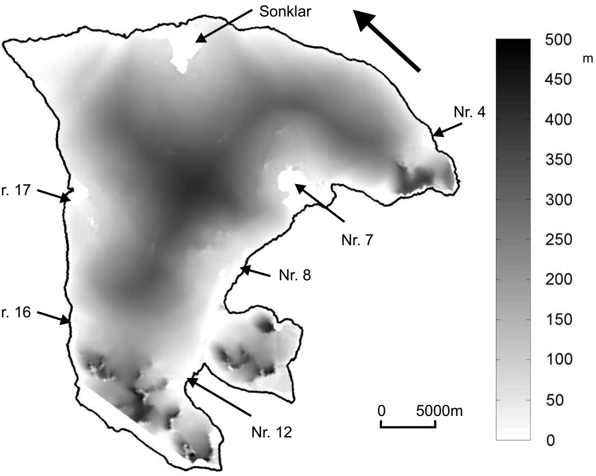

Figure 7: DSM of Hall Island derived from the interferometric phase. The black arrow indicates the viewing direction of the sensor. The positions of the largest outlet glaciers are indicated.

Standard deviations for the height values are extracted from the covariance matrix $\hat{K}_{\hat{x}\hat{x}}$, which is estimated within the adjustment. $\hat{K}_{\hat{x}\hat{x}}$ is defined by

$$\hat{K}_{\hat{x}\hat{x}} = \hat{\sigma}_0^2 Q_{\hat{x}\hat{x}} = \hat{\sigma}_0^2 \left(A^T P_{bb} A\right)^{-1} \text{ with } \hat{\sigma}_0^2 = \frac{\hat{\varepsilon}^T P_{bb} \hat{\varepsilon}}{n - u} \tag{10}$$

Equation (10) shows that the standard deviations of the adjusted unknowns are a function of the a priori defined functional and stochastic model as well as of the variance factor $\hat{\sigma}_0^2$, which is estimated within the adjustment. $\hat{\sigma}_0^2$ may be interpreted as link between the implemented models and the real data. Its values indicate how far the chosen functional and stochastic model fit the measured data sets. In the adjustment the a priori value of $\sigma_0^2$ is set to 1. Significant deviations of $\hat{\sigma}_0^2$ from 1 indicate errors in the models or gross errors in the data. A separate variance factor is estimated for each of the 14×14 tiles.

The standard deviations of the adjusted topographic heights are presented in Figure 8, split into the theoretical standard deviations (diagonal elements of matrix $Q_{\hat{x}\hat{x}}$) and the estimated variance factors for each of the 14×14 tiles. The parted representation entails several advantages. The theoretical standard deviations offer an insight into the properties of the adjustment's configuration (compare Figure 8*a*)). They illustrate the spatial distribution of the achievable height accuracy assuming a precise functional and stochastic model. Figure 8*a*) shows that the design of the adjustment allows to estimate topography with high accuracy all over the island. The estimated variance factors presented in Figure 8*b*) indicate, in which parts of the island the measured data sets are sufficiently described by the implemented models. Low values for $\hat{\sigma}_0^2$ appearing in large parts of the Moscow Ice Dome depict good agreement between model and data. Large values, which are visible in mountainous areas and in the catchment of the glaciers Sonklar, Nr. 7 and Nr. 8, indicate model errors. In the mountainous areas this errors are due to phase unwrapping problems. In the glacier catchments this errors are caused by an insufficient flow model.

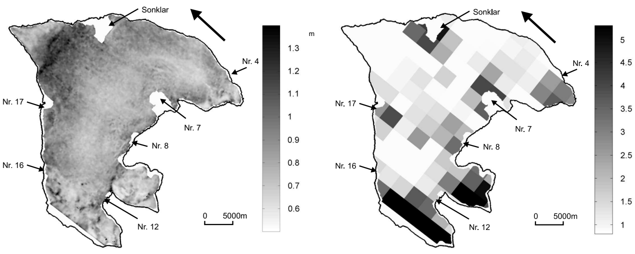

*a*) *b*)

Figure 8: *a*) Theoretical standard deviations of the estimated DSM [m]. *b*) Adjusted variance factors for Hall Island. One variance factor ist estimated for each of the 14×14 tiles.

The real standard deviations of the estimated topographic heights (diagonal of $\hat{K}_{\hat{x}\hat{x}}$) reach $\sigma_h \approx 1$ m to $\sigma_h \approx 2$ m in the glaciated terrain and lie between $\sigma_h \approx 2$ m and $\sigma_h \approx 8$ m in mountainous areas. In glaciated regions the standard deviations are in the range of the theoretical values estimated in Section 3 on the basis of theoretical data. Due to model errors the standard deviations in mountainous terrain are larger than the simulated ones.

**4.2.2 Velocity field of Moscow Ice Dome** To the best of the author's knowledge no detailed velocity map of the glaciers on Hall Island has been published up to now. Thus, the results of these study provide a new insight into the rheology and the physical properties of the ice masses on Hall Island. The estimates for the line-of-sight velocity components of the Moscow Ice Dome are presented in Figure 9. The surface velocity is given in m/a. As expected mainly the glaciers Sonklar, Nr. 7, Nr. 8, Nr. 12, Nr. 16 and Nr. 17 are reflected in the interferometric phase. This is because the flowing direction of these glaciers is approximately directed in the sensor's line-of-sight. Besides, the movement of

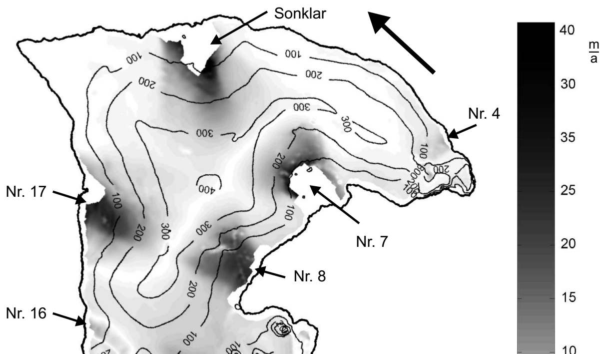

Figure 9: Velocity field of Hall Island derived from the interferometric phase. The black arrow indicates the viewing direction of the sensor. The positions of the largest outlet glacier are indicated.

glacier Nr. 4 is visible in addition. The transition from stable to moving ice is smooth for all glaciers. The absolute value of the line-of-sight velocities of Moscow Ice Dome varies from 0 m/a in ice-free areas and in the center of the island up to 43 m/a near the front of some of the outlet glaciers. The velocity of all glaciers increases from the center of the island towards the glacier terminus. The frontal part of the largest outlet glaciers suffers from strong temporal decorrelation. Thus, processing of glaciers velocities in the frontal parts of some glaciers was not possible.

The standard deviation of the line-of-sight velocity field is shown in Figure 10. The parameters are again separated into two parts, the theoretical standard deviations (Figure 10*a*)) and the a posteriori variance factors (Figure 10*b*)). Figure 8*b*) and 10*b*) are identical. Nevertheless, the parameters are presented for the sake of completeness. The distribution of theoretical standard deviations of the estimated velocities differs from the structure of the according topography values. This is due to the fact, that velocity estimates are mainly defined by interferograms with short baselines, whereas topography is especially influenced by interferograms with long baselines. In glaciated regions the real standard deviations (diagonal of $\hat{K}_{\hat{x}\hat{x}}$) of the velocity estimates vary between 0.1 m/a and 0.7 m/a and are in the range of the theoretical values estimated in Section 3. Due to model errors the standard deviations in mountainous terrain are larger than the simulated ones.

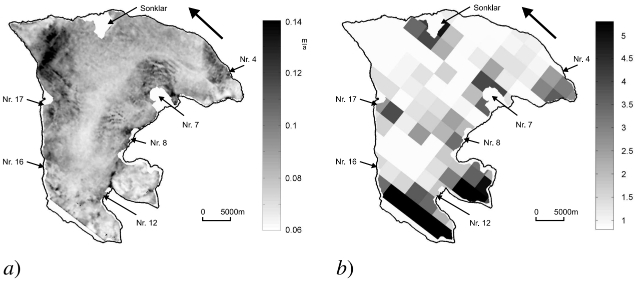

*a*) *b*)

Figure 10: *a*) Theoretical standard deviations of the estimated velocity field [m/a]. *b*) Adjusted variance factors for Hall Island. One variance factor ist estimated for each of the 14×14 tiles.

### 4.3 Interpretation of the residuals

During the estimation process several gross errors and model errors may occur that differ in origin and caused effect. Errors during SAR data acquisition, processing and phase unwrapping, wrongly determined stochastic properties, and insufficient functional relations are the most prominent. Hence, the development of a reliable estimation method, which allows to reveal gross errors in the data, is one of the most important goals of system design. The properties of the presented method regarding robustness and reliability are analyzed based on several indicators. All of them base on the equation

$$\Delta\hat{\varepsilon} = -\left(Q_{bb} - A(A^T P_{bb} A)^{-1} A^T\right) P_{bb}\Delta b = -\Upsilon\Delta b \tag{11}$$

that describes how gross errors in the observations and model errors $\Delta b$ are reflected in the vector of adjusted residuals $\hat{\varepsilon}$. The matrix $\Upsilon$ that maps $\Delta b$ onto the vector of adjusted residuals is presented in Figure 11. The structure of matrix $\Upsilon$ entails some convenient properties. The diagonal elements of $\Upsilon$ are close to unity, thus gross errors have a strong impact on $\hat{\varepsilon}$ and are therefore easily detectable. The off-diagonal elements are small. Hence, an error in observation $i$ only affects its associated residual and a dispersion of errors doesn't occur.

Because of this properties of the approach the vector of residuals $\hat{\varepsilon}$ can be consulted for analyzing gross errors in the data and the models. An analysis of $\hat{\varepsilon}$, which results during the estimation process indicates evidence for several error sources. These are

- Phase unwrapping errors, mainly in mountainous regions
- Non-modeled changes of the glacier topography in small isolated areas
- Errors due to an insufficient flow model in the caption of Sonklar Glacier
- Low frequency phase variations due to atmospheric effects

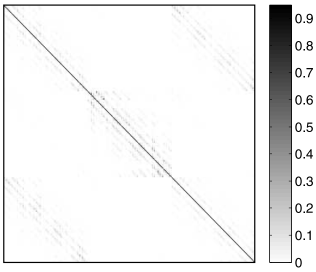

Figure 11: Structure of matrix $\Upsilon$ for a subset of the area of interest consisting of 10×10 pixel size.

## 5 SUMMARY

The presented approach allows an improved separation of topography- and displacement-related contributions to the interferometric phase by combining multi-temporal SAR interferograms in a least squares adjustment. The interpretability of the adjusted parameters is significantly increased by a systematic model-based quantification of all influences on the interferometric signal. The capability of the method to improve the accuracy of topography and displacement estimates, as well as the possibility to reveal gross errors in the observations has been demonstrated. A brief analysis of possible error sources has been presented. A validation using real data from an island in the Russian arctic confirms the approach.

## REFERENCES

Bamler, R. and Hartl, P., 1998. Synthetic Aperture RADAR Interferometry. Inverse Problems 14, pp. R1–R54.

Fatland, D. and Lingle, C., 1998. Analysis of the 1993-95 Bering Glacier (Alaska) surge using differential SAR interferometry. Journal of Glaciology 44(148), pp. 532–546.

Frolich, R. and Doake, C., 1998. Synthetic aperture radar interferometry over Rutford Ice Stream and Carlson Inlet, Antarctica. Journal of Glaciology 44(146), pp. 77–92.

Gray, A., Mattar, K., Geudtner, D. and Vachon, P., 1997. Experiments at the CCRS using ERS tandem mode data. Proceedings of 3rd ERS Symposium, Florence.

Hanssen, R., 2001. Radar Interferometry: Data Interpretation and Error Analysis. Vol. 2, 1 edn, Kluwer Academic Publishers.

Hoen, E., 2001. A correlation-based approach to modeling interferometric RADAR observations of the Greenland ice sheet. PhD thesis, Department of Applied Physics, Stanford University.

Lee, J.-S., Hoppel, K. and Mango, S., 1994. Intensity and Phase Statistics of Multilook Polarimetric and Interferometric SAR Imagery. IEEE Transactions on Geoscience and Remote Sensing 32(5), pp. 1017–1028.

Mikhail, E., 1976. Observations and Least Squares. IEP New York.

Vinogradov, O. and Psaryova, T., 1965. Katalog lednikov SSSR - Zemlya Frantsa-Iosifa. Vol. 3, Gidrometeoizdat Press, Moskau.